The large-scale dynamics of near-wall turbulence

By JAVIER JIMÉNEZ[1,2], JUAN C. DEL ÁLAMO[1] AND OSCAR FLORES[1]

[1]School of Aeronautics, Universidad Politécnica, 28040 Madrid, Spain
[2]Centre for Turbulence Research, Stanford University, Stanford, CA 94305, USA

The dynamics of the sublayer and buffer regions of wall-bounded turbulent flows are analysed using autonomous numerical simulations in which the outer flow, and on some occasions specific wavelengths, are masked. The results are compared with a turbulent channel flow at moderate Reynolds number. Special emphasis is put on the largest flow scales. It is argued that in this region there are two kinds of large structures: long and narrow ones which are endogenous to the wall, in the sense of being only slightly modified by the presence or absence of an outer flow, and long and wide structures which extend to the outer flow and which are very different in the two cases. The latter carry little Reynolds stress near the wall in full simulations, and are largely absent from the autonomous ones. The former carry a large fraction of the stresses in the two cases, but are shown to be quasi-linear passive wakes of smaller structures, and they can be damped without modifying the dynamics of other spectral ranges. They can be modelled fairly accurately as being infinitely long, and it is argued that this is why good statistics are obtained in short or even in minimal simulation boxes. It is shown that this organization implies that the scaling of the near-wall streamwise fluctuations is anomalous.

1. Introduction

This paper deals with the large-scale organization of the sublayer and buffer regions of wall-bounded turbulent flows. The companion paper by del Álamo *et al.* (2004*b*) extends the discussion to the logarithmic and outer layers. The interactions between the two regions are described in one or in the other paper, depending on where the data fit more naturally.

The small structures in the near-wall layer below $y^+ \approx 80$ scale approximately with the friction velocity u_τ and with the kinematic viscosity ν, and Jiménez & Pinelli (1999) showed that they change little in autonomous wall flows which have been modified to remove all the vorticity fluctuations from the outer flow. Their 'unit cell' is formed by a short stretch of a velocity streak and by a pair of quasi-streamwise vortices, such as those described by Robinson (1991). Their characteristic streamwise and spanwise length scales are $\lambda_x^+ \times \lambda_z^+ \approx 400 \times 100$, and they move with an advection velocity $c^+ \approx 10$. Fully nonlinear individual structures of similar sizes have been isolated by different methods in simplified Poiseuille (Jiménez & Moin 1991; Jiménez & Simens 2001; Waleffe 2001) and Couette flows (Nagata 1990; Waleffe 1998; Kawahara & Kida 2001). The intuitive reason for their scaling is that the impermeability condition constrains the wall-normal velocity and length scales, but Townsend (1976) noted that no such constraint exists for the wall-parallel velocity fluctuations, u and w, which

can be large. He called those hypothetical structures 'inactive' because they cannot, by themselves, generate Reynolds stresses. Because the inactive structures contain energy without contributing shear stress, they can degrade the strict wall scaling of the fluctuations.

There is experimental evidence that the near-wall scaling is only imperfect. In the logarithmic and upper buffer layers there are very large structures, much longer or wider than they are tall, which scale at least in part with the boundary layer thickness h (Perry, Henbest & Chong 1986), and other features of the buffer layer, such as the period between 'bursts', also scale partly in outer units (Laufer & Narayanan 1971; Shah & Antonia 1989). Hites (1997) measured the longitudinal velocity spectrum in boundary layers over a wide range of Reynolds numbers, and found that above $y^+ \approx 40$ the streamwise velocity spectrum is bimodal, with a shorter peak whose wavelength scales in wall units and a longer one that scales in outer units. His conclusions are supported by Österlund *et al.* (2000) using spectra from Österlund (1999), as well as by the results of Kim & Adrian (1999) and Morrison *et al.* (2002*a*) in pipe flows above $y^+ = 50$. Older data to the same effect were summarized by Jiménez (1998).

This longer spectral peak is missing below the buffer layer, but Hunt & Morrison (2000) noted that, since long structures contain a substantial part of the turbulent kinetic energy of the overlying logarithmic region, they should influence the sublayer. Because the ratio between the boundary layer thickness and the viscous wall length scale is the friction Reynolds-number $Re_\tau = u_\tau h/\nu$, this interaction between layers should appear as a large-scale effect in the high-Reynolds-number limit. Although less clear than for the upper buffer layer, there is also evidence for Reynolds-number effects in the lower buffer layer and in the sublayer. Metzger & Klewicki (2001) compared spectra at $y^+ = 15$ in two boundary layers with $Re_\theta = 2000$ and 5×10^6, and found a substantial excess of low-frequency energy in the latter with respect to the former. DeGraaff & Eaton (2000) made a comparative study of several boundary layers in a range of Reynolds numbers similar to those of Hites (1997), and found that the intensity of the near-wall peak of the longitudinal velocity fluctuations increases slowly with Reynolds number. Metzger *et al.* (2001) extended these results to the atmospheric boundary layer, and Morrison *et al.* (2002*b*) to high-Reynolds-number pipes.

Figure 1 shows longitudinal spectra of the streamwise velocity at $y^+ = 20$, and confirms this large-scale effect. The contours corresponds to individual premultiplied spectra which have been stacked together as a function of their Reynolds numbers, and which are treated as if they were a single function of Re_τ and of the streamwise wavelength $\lambda_x = 2\pi/k_x$. The upper block in the figure corresponds to the boundary layers in Hites (1997), while the lower one corresponds to three numerical channels by del Álamo *et al.* (2004*a*). The single spectrum between the two blocks will be discussed below.

The short-wavelength spectral peak scales relatively well in wall units as $\lambda_x^+ \approx 1000$, but the long-wavelength edge of the spectra moves to the right as the Reynolds number increases, approximately by ten times the boundary layer thickness or the channel half-width. Note that the longest wavelengths, of the order of 10^4–10^5 wall units, are at least an order of magnitude longer than the classical buffer-layer streaks.

The explanation mentioned above that these long structures are the near-wall reflections of the outer flow is plausible, but the possibility that the wall organizes itself cannot be discounted. Large-scale self-organization is a common feature of many nonlinear systems. The main goal of this paper is to determine how much of
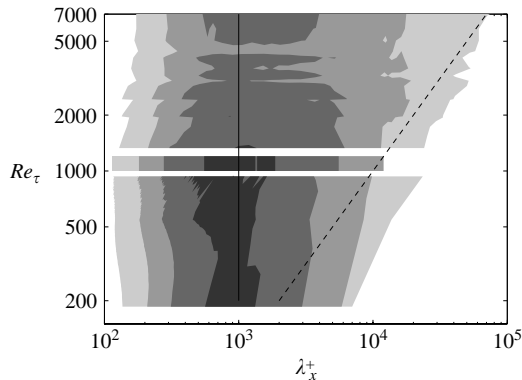
FIGURE 1. Longitudinal energy spectra for various near-wall flows. $y^+ = 20$. Grey levels correspond to the one-dimensional premultiplied spectra $k_x E_{uu}^{1D}/u_\tau^2$, as a function of the wavelength $\lambda_x = 2\pi/k_x$, and of the Reynolds number. The contours are equidistant with respect to the global maximum of all the spectra. Each line corresponds to a different Reynolds number. The upper block of contours is interpolated from fifteen boundary layers (Hites 1997). The lower one is interpolated from three numerical channels (del Álamo & Jiménez 2003; del Álamo *et al.* 2004*a*). The middle line is the autonomous wall computation C1 on table 1, whose Reynolds number has been assigned arbitrarily to fit into the available gap. The dashed line is $\lambda_x = 10h$, where h is either the channel half-height or the boundary layer thickness, and the solid one is $\lambda_x^+ = 1000$.

the large-scale organization of the inner layer is autonomous and how much is due, in full turbulent flows, to the influence of the outer region. We also seek to clarify the structure of the autonomous component. This is done by analysing numerical experiments in which the outer flow is removed, and by comparing them with a full-depth turbulent simulation at moderate Reynolds number.

The paper is organized as follows. The numerical technique used to isolate the wall region is described in §2. The results, with special emphasis on the similarities and differences between the large-scale spectral characteristics of the autonomous and of the full flows, are discussed in §3. Dynamical aspects and further analysis are presented in §4, and conclusions are offered in §5. A preliminary report of some of the results in this paper is Jiménez, Flores & García-Villalba (2001).

2. The numerical experiments

The numerical scheme used for the autonomous simulations is similar to that described by Jiménez & Pinelli (1999) and by Jiménez & Simens (2001), but the slightly modified version described here should be preferred to the previous ones. The Navier–Stokes equations are integrated in the form of evolution equations for the wall-normal vorticity ω_y and for the Laplacian of the wall-normal velocity $\phi = \nabla^2 v$, as described in detail by Kim, Moin & Moser (1987), using a pseudospectral code with dealiased Fourier expansions in the two wall-parallel directions, x and z, and either even or odd Chebychev polynomials in y.

Although the choice of the evolution variables, both of which are related to the vorticity, is essentially numerical, they have an interpretation that will later be useful. All the other flow variables are enslaved to them by linear relations which are local in time and in spectral space. The Fourier coefficients $\widehat{v}(y)$ of the normal velocity are for example solutions of Helmholtz problems in which the forcing is $\widehat{\phi}(y)$ and, because v

is predominantly generated near the wall by the streamwise vortices (Robinson 1991), we will associate the evolution of ϕ or of v with the dynamics of the vortices.

In the same way, the Fourier coefficients of the streamwise velocity component are

$$\widehat{u} = \frac{ik_x}{|k|^2}\partial_y\widehat{v} - \frac{ik_z}{|k|^2}\widehat{\omega}_y, \tag{2.1}$$

where $|k|^2 = k_x^2 + k_z^2$. For the elongated structures which will be of interest here, $k_z \gg k_x$. The first term in the right-hand side of (2.1) is then negligible, and ω_y measures the spanwise inhomogeneity of u. We will therefore associate ω_y with the streaks.

At each time step the right-hand sides of the two evolution equations are multiplied by a damping mask $1 - \Delta t\, F(y)$, where

$$F(y) = 0 \quad\text{if}\quad y \leqslant \delta, \qquad F(y) = 1/T \quad\text{if}\quad y \geqslant \delta_2 = 1.5\delta, \tag{2.2}$$

with the two limits connected smoothly by a cubic spline. Each time step can be written schematically as

$$\omega(t + \Delta t) = [\omega(t) + \Delta t\, N(t)][1 - \Delta t\, F(y)] \approx \omega(t) + \Delta t[N(t) - F(y)\omega(t)], \tag{2.3}$$

where ω stands for any of the two evolution variables, and N represents the full $\partial_t\omega$ from the Navier–Stokes equations, which are not modified below δ. To the lowest order (2.3) is the discretization of

$$\partial_t\omega - N = -F(y)\omega. \tag{2.4}$$

In this interpretation, T acts as a damping time independent of the length scale of the fluctuations and, when compared with the viscous damping time λ^2/ν for fluctuations of size λ, it defines a cutoff length $\lambda_c^+ = (T^+)^{1/2}$. Vorticity fluctuations shorter than λ_c are predominantly damped by viscosity, and longer ones are damped by the numerical mask. In this paper $T^+ \approx 1$, and all the fluctuations in the masked layer are suppressed by the mask. Irrotational fluctuations are not affected, and the outer edge of the Navier–Stokes layer merges into a potential core which prevents the formation of viscous boundary layers at the mask boundary.

The flows in Jiménez & Pinelli (1999) and Jiménez & Simens (2001) were integrated at constant mass flux in a channel, driven by a variable pressure gradient. This led to long integration times, because of the slow viscous evolution of the laminar flow above the mask, and added an extra parameter with no clear physical interpretation. The pressure gradient is substituted here by a constant shear stress imposed at the upper computational boundary. No-slip impermeable boundary conditions are imposed at $y = 0$, and the velocities are matched to the outer potential fluctuations at the edge of the computational domain, $y = 1$, using the method of Corral & Jiménez (1995).

The mask height is adjusted so that the vorticities are essentially zero at the edge of the computational domain, and their wall-normal spectral expansions remain accurate. The expansions of the variables extending into the potential region, such as the velocities, are supplemented by exponentials. The coefficient of the $\exp[i(k_x x + k_z z)]$ Fourier component of v is, for example, expanded in terms of odd Chebychev polynomials plus two extra basis functions,

$$\exp\left[\pm\left(k_x^2 + k_z^2\right)^{1/2}y\right], \tag{2.5}$$

which describe its irrotational component. Their coefficients are adjusted to satisfy the impermeability condition at $y = 0$ and the vanishing of the fluctuations as $y \to \infty$.

The $(0, 0)$ Fourier modes of u and w cannot be expressed in terms of ω_y and ϕ, and are not modified by the numerical mask. In their expansions the exponentials are

Case	δ^+	L_x^+	L_z^+	Δx^+	Δz^+
C1	72	12, 000	2000	13	7.5
C2	60	12, 000	1000	13	7.5
C3	72	6, 000	1000	13	5
F0	550	14, 000	7000	13	7.5

TABLE 1. Parameters of the autonomous simulations used in the text. The case F0 is a full-channel simulation by del Álamo & Jiménez (2003), used for comparison, in which δ is the half-height. The resolutions Δx and Δz are given after dealiasing.

replaced by linear functions,

$$a_0 + b_0 y. \tag{2.6}$$

The linear mean velocity profile in the region of irrotational fluctuations reflects the absence of a mean pressure gradient. The constant a_0 is determined by the wall boundary condition. The slope b_0 is zero for w, and defines for u the constant spatially averaged wall friction.

In all the experiments in this paper $b_{0,u}$ is scaled so that the height of the computational domain is $y^+ = 120$. Note however that this is not physically relevant, because the mask determines the largest possible wall-normal extent of the turbulent structures. The only relevant turbulent Reynolds number is $\delta^+ = u_\tau \delta / v$.

Since our goal is to study the large-scale organization of the flow, the simulations are performed in computational boxes whose streamwise and spanwise periodicities are long, $L_x^+ \approx 1.2 \times 10^4$, and wide, $L_z^+ \approx 10^3$. The comparatively narrow spanwise box size was found not to interfere with the structures, which are narrow in the autonomous simulations. A simulation in a box twice as wide did not show any differences with the narrower one. The resolution is in most cases $\Delta x^+ = 13$ and $\Delta z^+ = 7.5$, resulting in 1536×192 collocation points for the case mentioned above. The wall-normal expansion, which is not dealiased, uses 49 Chebychev modes. The first collocation point is $y^+ = 0.06$. While this resolution was found to be sufficient for the large-scale structures, it results in some spanwise truncation of the vorticity spectra, specially around $y^+ \approx 40$. A few simulations were run at the higher spanwise resolution $\Delta z^+ = 5$. No appreciable differences were found in the velocity profiles or spectra, but all our discussions for the vorticity use the higher-resolution simulations. A summary of the principal computational experiments can be found in table 1. The reference channel F0 is also computed in a large box, $8\pi \times 2 \times 4\pi$, and its adequacy with respect to the large structures is discussed by del Álamo & Jiménez (2003).

Because of the lack of either mean spatial growth or of a pressure gradient, these autonomous simulations do not correspond directly to the wall region of any turbulent flow, except perhaps to a single wall in a Couette flow. Their closest analogue would be the wall region of either boundary layers or channels at infinitely large Reynolds numbers, but there is nothing in them equivalent to the infinitely long outer scales of full flows in that limit. Any large scales in the autonomous systems have to be generated by the wall itself.

3. Results

Most of the experiments in this paper use $\delta^+ = 72$, but a few were run at $\delta^+ = 60$ to check the effect of the mask. The resulting turbulence statistics are compared in figure 2 with the full channel F0. The mean velocity shows a short 'logarithmic' layer
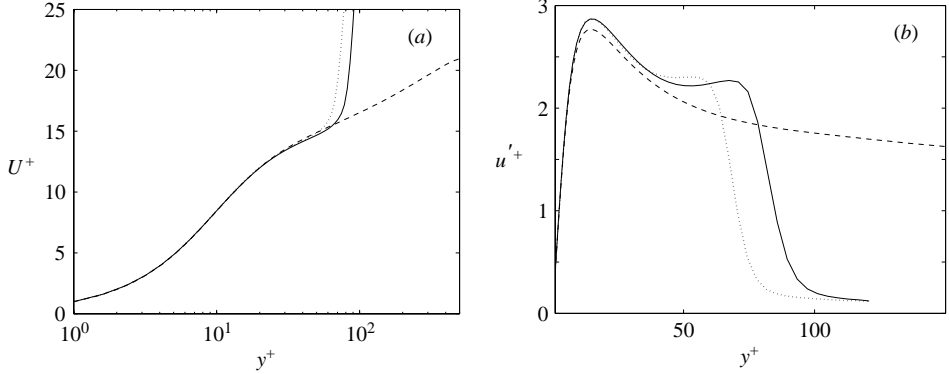
FIGURE 2. Mean profiles for: ———, the autonomous simulation C1, with $\delta^+ = 72$; ········, the autonomous case C2, $\delta^+ = 60$; ----, the full channel F0, with $Re_\tau = 550$. (a) Mean velocity. (b) Streamwise velocity fluctuations.

before joining the linear profile of the irrotational region, and the velocity fluctuations agree reasonably well with the full-channel results up to about half the mask height. The peak of the fluctuations just above δ is an artifact of the damping, and was described by Jiménez & Simens (2001). The results for other quantities are similar to those in the figure, and from now on we will only discuss the $\delta^+ = 72$ cases below $y^+ \approx 40$.

Figure 3 displays two-dimensional spectral densities, $E^{2D}(\lambda_x, \lambda_z)$, for the full and autonomous flows. The first surprise is the almost perfect correspondence between the two cases, specially for the wall-normal velocity component, whose structures are relatively short and narrow. The second one is that the large structures of the streamwise velocity, and to a certain extent those of w, are longer in the autonomous flow than in the full channel. Both results contradict the models in which the outer flow is the origin of the near-wall large scales, since there are no turbulent fluctuations above $y^+ \approx 80$ in the autonomous case. The longitudinal one-dimensional spectrum of u in the autonomous flow C1 has been included in the compilation in figure 1 as the isolated line in the gap between the boundary layers and the channels. The Reynolds number assigned to it, $Re_\tau \approx 1000$, is arbitrary, since we have seen that the only relevant one would be $\delta^+ \approx 72$. It emphasizes that the autonomous spectrum is much longer than what could be expected from its flow thickness. Longer computational boxes were beyond our computational resources, but all our experiments with shorter boxes suggest that the autonomous spectra extend to fill the whole length of any simulation.

The longer scales are also wider, and very anisotropic, as shown by the location of the spectra with respect to the locus of wall-parallel isotropy included in figure 3. This is specially true for the streamwise velocity and for the Reynolds stresses, whose spectral 'ridges' follow fairly well the power law

$$\lambda_z^+ / \lambda_x^{+1/3} = 13. \tag{3.1}$$

The spectra of the other two velocity components are closer to isotropic, but a trace of (3.1) is found in w, specially in the autonomous simulation.

The wall-normal structure of the spectral distributions is shown in figure 4. Individual one-dimensional spectra, $E^{1D}(\lambda)$, are obtained by summing $E^{2D}(\lambda_x, \lambda_z)$ either over the spanwise or over the streamwise wavenumbers, and are represented
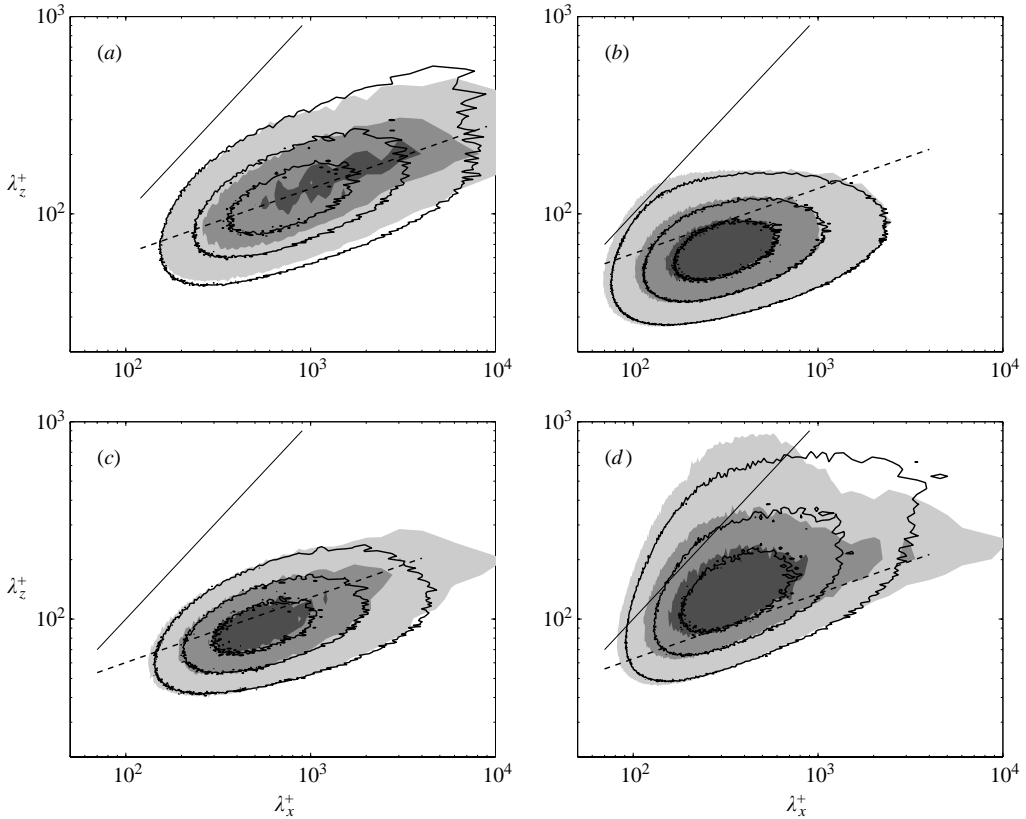
FIGURE 3. Premultiplied two-dimensional velocity spectra and cospectra, $k_x k_z |E^{2D}(\lambda_x, \lambda_z)|/u_\tau^2$, as functions of the streamwise and spanwise wavelengths. $y^+ = 16$. The shaded contours are the autonomous simulation C1. The lines are the full turbulent channel F0. The solid straight lines are $\lambda_x = \lambda_z$, and correspond to horizontally isotropic structures. The dashed straight lines are $\lambda_z^+/\lambda_x^{+1/3} = 13$, as in (3.1). The contours are (0.25, 0.5, 0.75) times the maximum value of the corresponding spectrum for the full channel. (*a*) Streamwise velocity. (*b*) Wall-normal velocity. (*c*) Reynolds-stress cospectrum. (*d*) Spanwise velocity.

as functions of the wavelength and of the wall distance y. Again there is good correspondence between the autonomous and the full cases in the lower half of the unmasked layer. The vertical velocity is concentrated into structures for which $\lambda_x^+ \times \lambda_z^+ \approx 300 \times 50$, strongest near $y^+ = 40$, which will be seen in §4 to agree with the signature of the near-wall quasi-streamwise vortices. The streamwise velocity spectra are slightly wider and much longer, strongest at $y^+ = 10$–20, and can be interpreted as the signature of the near-wall streaks.

An important scale is defined by the peak of the Reynolds-stress cospectrum, which is shown in figures 4(*e*) and 4(*f*) multiplied by the gradient $\partial_y U$ of the mean velocity, to represent the spectral distribution of the turbulent energy production. It is concentrated below $y^+ = 30$, around $\lambda_x^+ \times \lambda_z^+ \approx 600 \times 100$. The secondary peak which appears above the mask in the autonomous simulation is due to the large velocity gradient in that region, and has no dynamical significance; all its energy is dissipated locally by the numerical mask. It is seen in figures 3(*c*) and 4(*e*) that the near-wall production extends to fairly long wavelengths, specially for the autonomous simulation. In fact, if we define 'long' structures as those longer than twice the
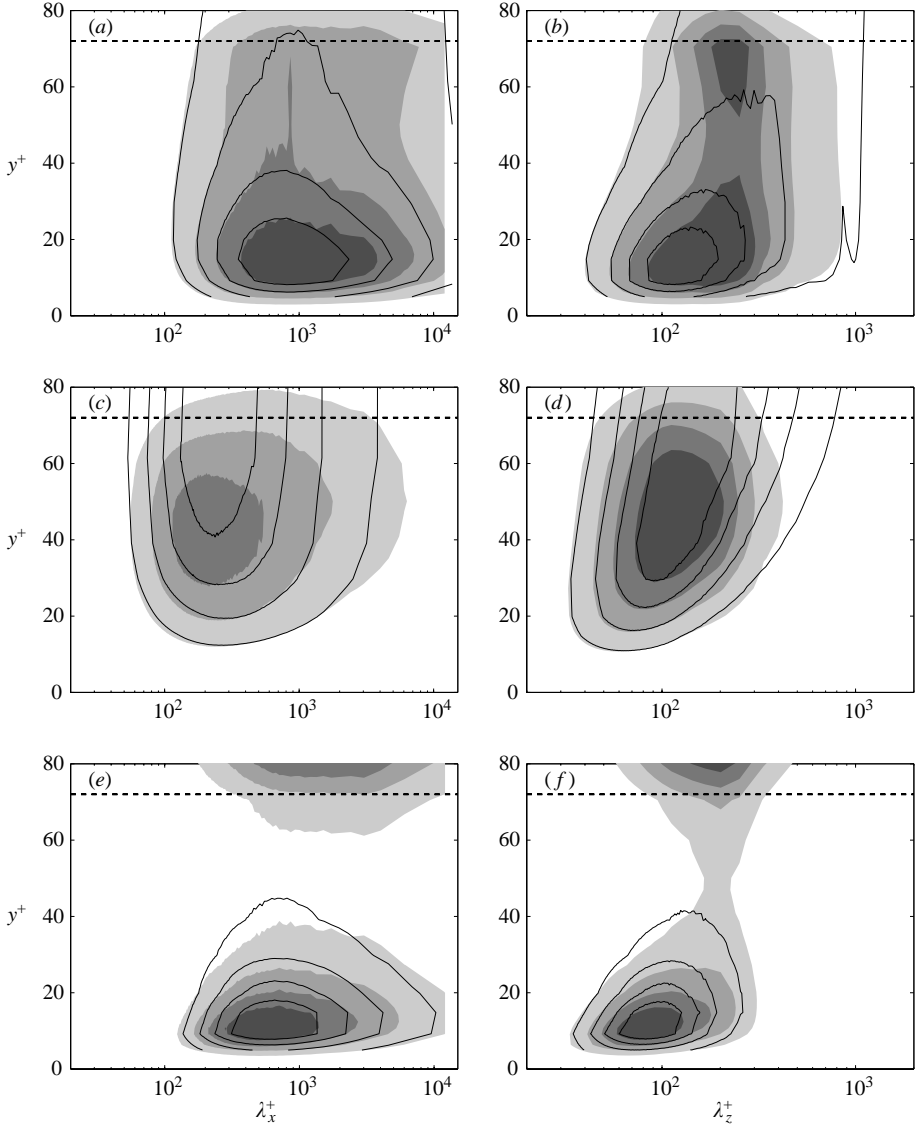
FIGURE 4. Premultiplied one-dimensional spectra, $kE^{1D}(\lambda)/u_\tau^2$, as functions of the wavelength and of the wall distance. The shaded contours belong to the autonomous simulation C1, and the lines to the full channel F0. The contours are uniformly spaced with respect to the overall maxima of the full-channel spectra. The dashed horizontal line is the lower limit of the numerical mask C1. (a,b) Streamwise velocity. (c,d) Wall-normal velocity. (e,f) Energy production cospectra, $-(\partial_y U)\,kE_{uv}^{1D}$. (a), (c) and (e) Streamwise spectra, and (b), (d) and (f) spanwise spectra.

production peak, $\lambda_x^+ \geqslant 1200$, they contain 51% of the energy of the streamwise velocity component below $y^+ = 40$, 53% of the Reynolds stresses and 49% of the energy production, but only 24% of the wall-normal energy. The corresponding numbers for the full channel are 51%, 46%, 44%, and 20%.

  The reason why the long structures carry Reynolds stresses, even with comparatively little vertical velocity, is that they are very organized, with a high correlation among
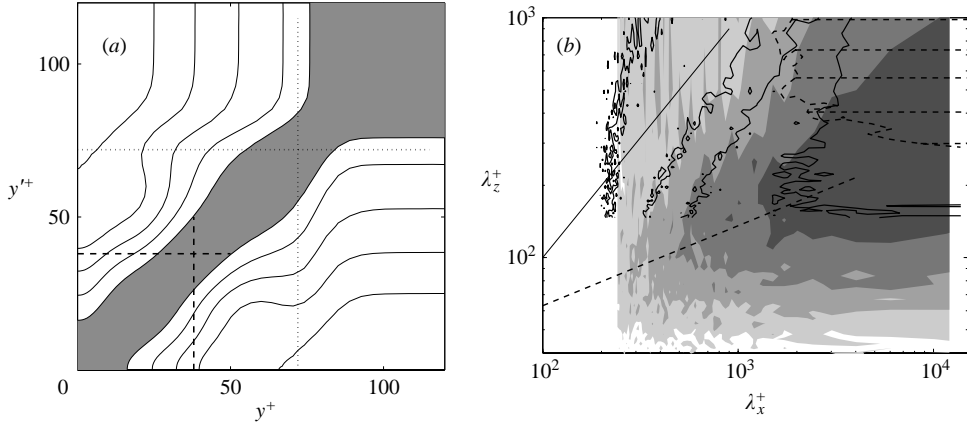
FIGURE 5. (a) Correlation coefficient C_{uu} for the mode $\lambda_x^+ = 3000$, $\lambda_z^+ = 140$. Contours are 0.5(0.1)0.9, and the shaded region is above 0.9. The dashed lines mark y_0 in (3.3), and the dotted lines are the mask height. (b) Coherence height $H_{uu}^+ = 30(2)36$. The shaded contours are case C1, and the lines are the full channel F0. The two straight lines are as in figure 3. The dashed contour is the region in which $C_{uu}(15^+, 0.5\delta) > 0.15$ for case F0.

their velocity components. The structure parameter $-E_{uv}/(E_{uu}E_{vv})^{1/2}$, not shown in the figure, is very close to unity in the spectral 'tail' of the production peak.

The large scales are also deep. The correlation coefficient between the individual Fourier coefficients $\hat{u}$ of the streamwise velocity at two wall distances is defined as

$$C_{uu}(k_x, k_z, y, y') = \frac{|\langle \hat{u}(k_x, k_z, y)\hat{u}^*(k_x, k_z, y')\rangle|}{(\langle |\hat{u}(k_x, k_z, y)|^2\rangle\langle |\hat{u}(k_x, k_z, y')|^2\rangle)^{1/2}}, \qquad (3.2)$$

where ()* stands for complex conjugation, and is also very close to unity for long and wide wavelengths. Note that the numerator in (3.2) is an absolute magnitude, instead of the more usual real part, and that C_{uu} is insensitive to any possible tilting of the structures. An example for a particular Fourier mode of the autonomous simulation is given in figure 5(a). Its correlation coefficient remains above 0.6 within the reliable region $y^+ < 40$, and never falls below 0.4 within the full depth of the computational domain. Figure 5(b) shows the spectral distribution of the 'coherence height' within a wall distance y_0, which is defined for each mode as

$$H_{uu}^2(k_x, k_z) = \int_0^{y_0} \int_0^{y_0} C_{uu} \, dy \, dy'. \qquad (3.3)$$

The integration height used for the integrals in the figure is $y_0^+ = 38$. All the modes in the upper-right-hand corner of the spectral plane, which corresponds to the spectral production tail, have correlation heights which are larger than $y^+ = 30$, and are therefore essentially coherent over the full integration height. That result is consistent with those of Bullock, Cooper & Abernathy (1978), who computed covariances for velocity signals filtered in different frequency bands. In a pipe at $Re_\tau = 2600$ they found that the correlation coefficient of u between $y^+ = 50$ and all the $y' < y$ was larger than 0.6 when $\lambda_x^+ \gtrsim 1000$, but that it vanished in the sublayer for the shorter wavelengths $\lambda_x^+ < 250$.

The modes that are correlated across all heights, from y to the wall, such as the one in figure 5(a), correspond to the 'attached' eddies proposed by Townsend (1976). Figure 5(b) shows that, when the heights considered are in the buffer region, the size
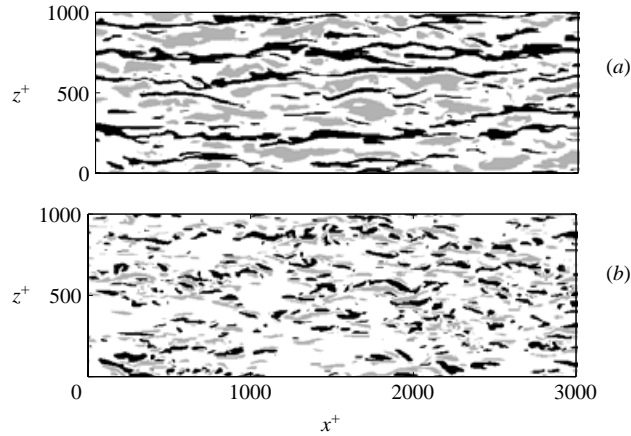
FIGURE 6. Structure of the velocity on a wall-parallel plane at $y^+ = 16$. Case C1. Both parts correspond to the same plane of the same snapshot, with the mean velocity from left to right. The black areas are below one standard deviation from the mean, and the light-grey ones are one standard deviation above. (*a*) Streamwise component. (*b*) Wall-normal component.

of the attached structures scales in wall units, $\lambda_x^+ \gtrsim 1000$ and $\lambda_z^+ \gtrsim 60$. For each y there is a attached spectral region, and it follows from the above definition that those farther from the wall are contained within the lower ones. In a kinematic sense the latter are influenced by the former, but not vice versa. Del Álamo & Jiménez (2003) and del Álamo *et al.* (2004*a*) found that the structures correlated across the full channel scale in outer units, $\lambda_x \gtrsim 5h$ and $\lambda_z \gtrsim h$. That region is represented for case F0 in figure 5(*b*) as the dashed contour, and it is where the autonomous and the full simulations disagree, precisely because of the outer structures are absent in the former.

4. Dynamics

4.1. *The wall-normal velocity*

The simplest interpretation of the large-scale organization of the wall-normal velocity is that, to lowest approximation, it has none. In the snapshots of the buffer layer in figure 6 the streamwise velocity is dominated by the familiar long streaks, while the wall-normal velocity contains only isolated active regions, roughly $300 - 500$ wall units long, randomly distributed over the plane. This difference in length between the two kinds of structures has been described qualitatively in essentially all the numerical simulations of the near-wall layer, and is for example already mentioned in the review by Robinson (1991). It will be made more quantitative in this section. The light and dark grey regions appearing side by side in figure 6(*b*) are sharp spanwise variations of v induced by the buffer-layer quasi-streamwise vortices. If we model the spanwise structure of v by a random array of zero-mean pairs of delta-functions separated in z by a distance $2b$, the resulting premultiplied spectrum is $k_z E_{vv}(k_z) \sim k_z \sin^2(k_z b)$†, which is maximum at $\lambda_z \approx 3.4b$. Comparing this value with the spanwise location of the maximum in figure 3(*b*), $\lambda_z^+ \approx 50$, we obtain a spanwise separation between upwash

---

† The Fourier transform of $\delta(z - b) - \delta(z + b)$ is $i\pi^{-1}\sin(kb)$, and convolving the dipole with a random array of deltas just multiplies the spectrum by a constant.
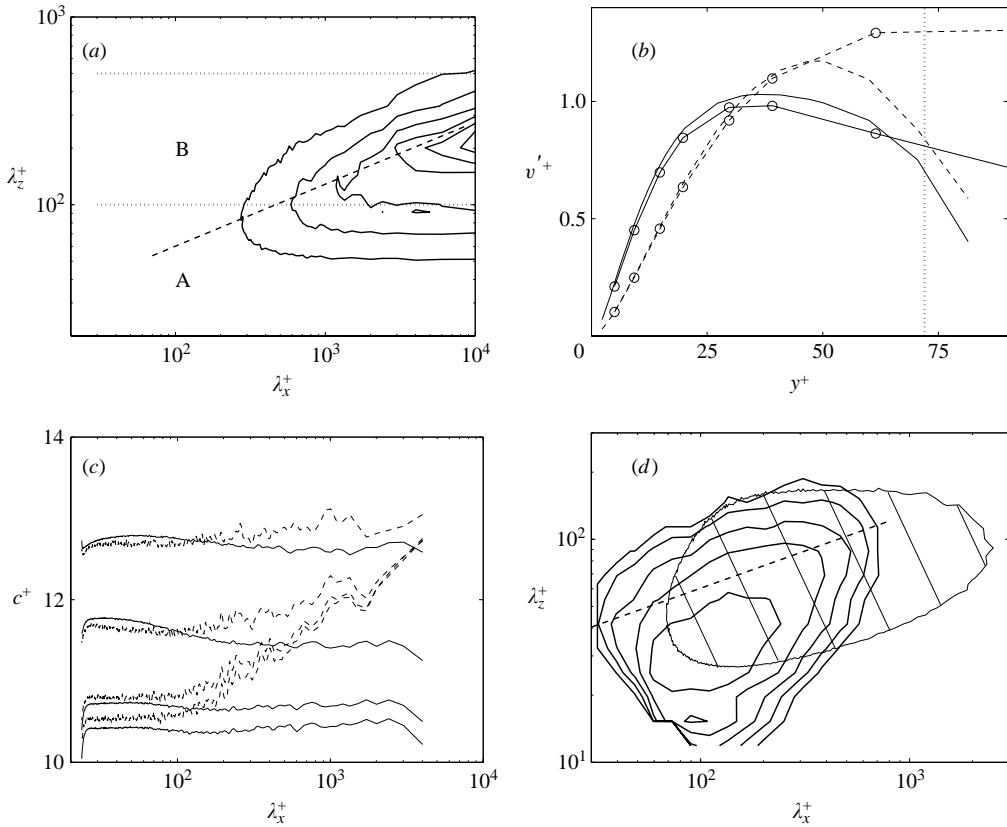
FIGURE 7. Case C1, $y^+ = 16$. (*a*) Two-dimensional spectrum of v, not premultiplied. (*b*) Wall-normal distribution of v', computed over spanwise spectral bands. The vertical dotted line is the mask height. ———, Band A in (*a*), $\lambda_z^+ = 20$–100; – – – –, band B, $\lambda_z^+ = 100$–500. Lines with symbols are from the full channel F0. (*c*) Advection velocity of individual modes for $\phi = \nabla^2 v$, plotted as a function of the streamwise wavenumber. Each line is averaged over one of the wall-distance bands $y^+ = 0(10)40$. Velocity increases with wall distance. Lines are as in (*b*). (*d*) P.d.f. of the logarithms of the longitudinal and lateral dimensions of the bounding rectangles for individual v-structures. The contours are logarithmically spaced by half an order of magnitude. The hatched region is the 0.25 contour of the premultiplied v spectrum in figure 3(*b*). The dashed straight lines in (*a*) and (*d*) are equation (3.1).

and downwash of $2b^+ \approx 30$, which is the diameter of the maximum azimuthal velocity isosurface of a streamwise Rankine vortex of radius $R^+ \approx 13$, in good agreement with the value obtained by Kim *et al.* (1987).

Several lines of evidence supporting this model are summarized in figure 7. Consider first the spectrum of v, which is shown in figure 7(*a*) without premultiplication. A spectral tail does not necessarily imply long structures. The spectrum of a random array of delta-functions is for example flat, and that of a random array of objects of size λ_0 is flat for $\lambda \gtrsim \lambda_0$. The horizontal contour lines towards the right-hand side of the figure represent such a flat spectrum, and suggest that v is formed by a random superposition of compact structures whose sizes lie roughly along the dashed line representing the power law (3.1).

Figure 7(*b*) shows the vertical distribution of the v-fluctuations, summed over spectral bands which have been drawn in figure 7(*a*). They are compared with those

in the full channel. The intensity of the narrow structures in band A peaks within the buffer region in both cases. They are the structures represented in figure 6(b). It can be shown that the vertical distribution of these fluctuations is the same for all the wavelengths longer than $\lambda_x^+ \gtrsim 300$, suggesting that they all refer to an array of structures of roughly that length. The wider scales in range B peak farther away from the wall, and they only agree with the full channel below $y^+ \approx 25$. They are the truncated remnants of structures which in the latter case are associated with the lower logarithmic layer.

Figure 7(c) displays the phase velocity of the Fourier modes of ϕ, averaged over bands of wall distance. The phase velocity is usually computed from the space–time spectrum, but we have used a different definition. A simple wave $\phi = \widehat{\phi} \exp[\mathrm{i}k_x(x-ct)]$, with phase velocity c, satisfies

$$c = \mathrm{Im}\frac{\langle \phi \, \partial_t \phi^* \rangle}{k_x \langle \phi \, \phi^* \rangle}, \tag{4.1}$$

where Im is the imaginary part. In more complicated situations (4.1) can still be used as a definition of the phase velocity and, since $\partial_t \phi$ is available from the equations of motion, it is usually more convenient in numerical simulations. Its relation with the more usual spectral definition (Wills 1964) is documented in del Álamo *et al.* (2004b), where it is compared with previous experiments.

The velocities in figure 7(c) are plotted for two different bands of spanwise wavelengths, which correspond to those in figure 7(b). For the narrower structures in band A, the phase velocity is essentially independent of λ_x, in agreement with the interpretation that all the Fourier modes in this band correspond to the same objects.

The velocities for the wider structures in band B behave differently. Below $\lambda_x^+ < 200$ they follow closely the results for the narrow modes, although it is clear from the spectrum that those short and wide modes contain very little energy. For longer wavelengths the phase velocity increases, and converges to a high value which is independent of the wall distance. This is the region which in figure 5 contains structures spanning the full buffer layer and spilling into the potential core. Their high advection velocities, which are higher in the autonomous than in the full simulations, are in the autonomous case representative of the mean velocities in the potential core. In the full simulations they are of the same order as the velocities in the logarithmic layer.

Kim & Hussain (1993) also found that the phase velocity of v was relatively insensitive to λ_x and increased weakly with λ_z, but their computational domain was too small to show the sharp growth of c for long and wide wavelengths. Krogstad, Kaspersen & Rimestad (1998) investigated a laboratory boundary layer at $Re_\tau \approx 600$, and found an increase of the advection velocities at roughly the same values as those in figure 7.

The overall model suggested by these observations is a random array of structures with characteristic sizes of the order of $\lambda_x^+ \times \lambda_z^+ = 300 \times 50$, presumably generated by the quasi-streamwise vortices, moving with a phase speed $c^+ \approx 10$. They contain the bulk of the energy of v below $y^+ = 50$. Wider v-structures exist, but they are taller and move faster, and they are linked to the flow above the buffer layer.

The size of the v-structures can be estimated directly by analysing flow snapshots such as those in figure 6(b). Each flow plane is segmented into regions in which v is above or below one positive or one negative standard deviation ($v^+ = \pm 0.59$). Those are then separated into individual connected objects, and inscribed into rectangles aligned with the flow. Connectivity is defined by the four orthogonal nearest
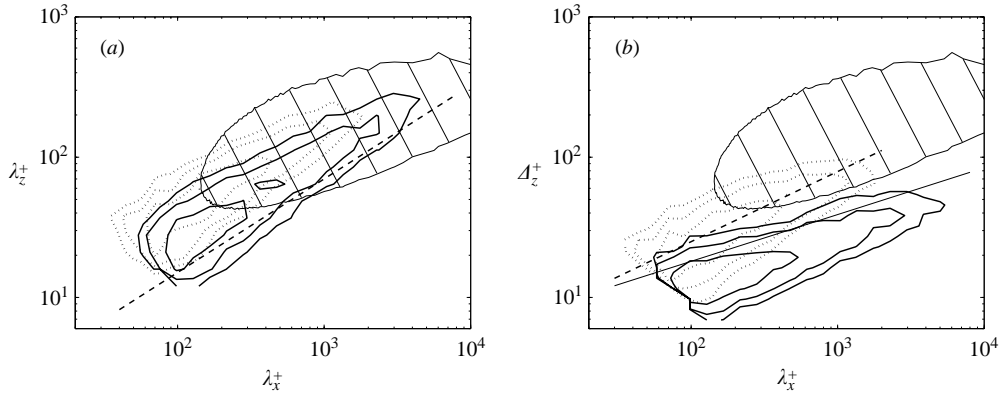
FIGURE 8. (*a*) P.d.f. of the logarithms of the longitudinal and lateral dimensions of the bounding rectangles for individual *u*-structures, as in figure 7(*d*): ———, low-velocity streaks; ········, high-velocity regions. The dashed straight line is (4.7). (*b*) Same as (*a*) for the width of the structures, computed from their areas. The solid straight line is (4.6) and the dashed one is (4.5). Case C1. $y^+ = 16$. The hatched region in both figures is the 0.25 contour of the premultiplied *u*-spectrum in figure 3(*a*).

neighbours. There is little difference at this wall distance between regions of positive and of negative *v*, and the p.d.f. of the widths and lengths of the bounding rectangles which is presented in figure 7(*d*) reflects their common distribution. It accounts for about 20% of the total area of the flow sections analysed. The diagonal cutoff in the lower-left corner of the figure is an artifact of the algorithm, which rejects structures smaller than 20 grid points as being too close to the numerical resolution.

The lengths and widths in figure 7(*d*) agree reasonably well with the peak of the premultiplied spectrum of *v*, which is included in the figure for reference, although the two quantities are only indirectly related. Sizes and spectral wavelengths are proportional but not identical and, for example, the premultiplied spectrum of a 'box' function of length *b* peaks at $\lambda_x = 2b$. Note that there are no structures longer than about 1000 wall units, and that their characteristic length is about 150^+. This supports the qualitative impression from figure 6(*b*) that the buffer-layer vortices are short structures, and the model developed above in which the *v*-spectrum is explained in terms of compact objects in its short-wavelength end.

The analysis described here was repeated for the full simulation F0, with essentially identical results.

4.2. *The streamwise velocity streaks*

The visual difference between the lengths of the *u*- and *v*-structures in figure 6 is confirmed by comparing the probability distributions of their bounding rectangles in figures 7(*d*) and 8(*a*). There is for *u* a clear difference between high- and low-velocity structures, which are defined as being beyond one standard deviation from the local mean velocity ($u^+ = 11 \pm 2.9$ at $y^+ = 16$). The high-velocity structures are shorter than the low-velocity streaks (Robinson 1991), but they are both at least 2 to 5 times longer than the structures of *v*. When the widths Δ_z of the structures are computed as their actual surfaces divided by their lengths, the high-velocity regions are found to be at most 100 wall units wide, while the width of the low-velocity streaks rarely exceeds 50 wall units (figure 8*b*). Visual inspection of individual objects in figure 6(*a*) shows
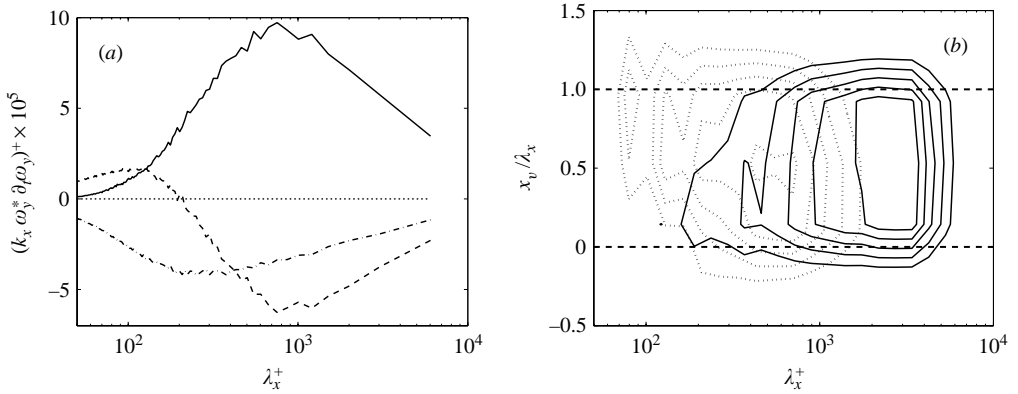
FIGURE 9. (a) Spectral distribution of the production terms for ω_y in (4.2). Case C3, for $100 \leqslant \lambda_z^+ \leqslant 500$, at $y^+ = 13$: ——, linear forcing, $(\partial_z \widehat{v}) \partial_y U$; - - - -, nonlinear advection; —·—·, viscous diffusion. (b) P.d.f. of the relative position of the v-structures within the bounding rectangles of the u-structures, plotted against the length of the u-structures. The p.d.f.s have been corrected for the logarithmic abscissae, and the contours are linearly spaced by 0.05. Case F0, $y^+ = 12$. Lines as in figure 8.

that the longest connected streaks are complex objects formed by the coalescence of several shorter ones.

It is generally agreed that streaks are formed by the distortion by v of the mean shear. The importance of this effect is shown in figure 9(a) by direct evaluation of the magnitude of the different terms in the evolution equation for $|\widehat{\omega}_y|^2$, which can be written as

$$\partial_t |\widehat{\omega}_y|^2/2 = -(\partial_y U)\,\mathrm{Im}(k_z\,\widehat{\omega}_y^*\widehat{v}) - \mathrm{Re}(\widehat{\omega}_y^* \widehat{N}_\omega) + Re^{-1}\mathrm{Re}(\widehat{\omega}_y^* \nabla^2 \widehat{\omega}_y), \qquad (4.2)$$

where Re and Im are the real and imaginary parts. The three terms on the right-hand side are the vertical advection of the mean velocity profile, the rest of the nonlinear advection term, and the effect of viscosity. The dominant term for the long scales is the linear forcing, which is balanced by the lateral nonlinear advection and by the viscosity, with the latter being negligible above $y^+ = 10$–15. Streamwise gradients are not important for structures longer than about $\lambda_x^+ = 300$, and the formation of the streaks takes place essentially by stirring of the mean shear in the (z, y) cross-plane, as modelled by Orlandi & Jiménez (1994).

This simple model can be used to explain several of the properties mentioned above. Consider a uniform shear, $u \sim y$, advected by a streamwise point vortex of circulation γ. In the cross-plane the streamwise velocity behaves as a passive scalar, and is deformed after a time t into

$$u \sim r\sin(\theta - \gamma t/2\pi r^2), \qquad (4.3)$$

where r and θ are polar coordinates centred on the vortex. A representative streak diameter can be defined by the outermost zero of u at $\theta = \pi$,

$$\Delta_z = \pi^{-1}(2\gamma t)^{1/2}. \qquad (4.4)$$

As it thickens, the streak also lengthens, and its high- and low-velocity sides evolve differently. Below $y^+ \approx 30$, where the vortices are located, the high-speed regions are characterized by a fairly sharp viscous shear layer near the wall, followed by a plateau where $U^+ \approx 15$. The low-speed structures have a roughly uniform shear

$S = \partial_y U^+ \approx 0.5$ across the whole layer. We have seen in the previous section that the vortices move with an advection velocity $c^+ \approx 10$. In the faster uniform flow of the high-speed regions they produce wakes which move ahead of them, whose lengths increase with time as $\lambda_x \approx |c^+ - U|t$. Substituting this estimate in (4.4), and assuming that $\gamma^+ = 150$ (Robinson 1991) and $U^+ - c^+ \approx 5$,

$$\Delta_z^+ \approx \pi^{-1}(2\gamma\lambda_x/|c^+ - U|)^{+1/2} \approx 2.5\lambda_x^{+1/2}. \tag{4.5}$$

In the sheared low-speed regions the vortices move faster than the flow, and the wakes are left behind them. The streak is deformed by the shear S, and its length is determined by the velocity difference between its top and its bottom, which can be roughly estimated as $\lambda_x = S\Delta_z t$ by assuming that the streak height is roughly equal to its width. Substituting in (4.4), the result is

$$\Delta_z^+ \approx (2\gamma\lambda_x/\pi^2 S)^{+1/3} \approx 4\lambda_x^{+1/3}. \tag{4.6}$$

Both (4.5) and (4.6) have been included in figure 8(b), and are reasonable approximations to the data. Except for the numerical coefficients, whose success is probably largely coincidental, (4.5) and (4.6) are dimensional results which could have been constructed using the viscosity ν instead of γ. A viscous origin for the observed power laws was proposed by Jiménez *et al.* (2001), but figure 9(a) shows that the process of streak formation is inviscid except very near the wall. Note that, because the low-speed streaks are the longest objects at any given width, (4.6) is essentially equivalent to the spectral power law (3.1).

A prediction of this model is that the v-structures should be preferentially located near the leading edge of the low-velocity streaks, and near the trailing edge of the high-velocity ones. This can be tested by computing the relative position of one along the other in the snapshots. A v-structure is associated with a given u-structure if their bounding rectangles intersect. For each v-structure the longitudinal position x_v of its centre of gravity with respect to the leading edge of the u-structure is computed, and normalized with the length of the u-structure. Low or negative values of x_v/λ_x correspond to v leading u, while $x_v/\lambda_x = 1$ represents the trailing edge of u. The results are summarized in the two p.d.f.s in figure 9(b). For long u-structures associated with several v-structures there is no positional preference, but for the shorter ones, which are presumably in the process of formation, v leads the low-velocity regions and trails the high-velocity ones, as predicted. It can also be shown that the longer streaks are more intense than the shorter ones, again supporting the model of their growth by continuous pumping by the vortices.

A rough analysis can also be carried out for the meandering of the streaks, as measured by the bounding rectangles whose dimensions are plotted in figure 8(a). As the streaks are formed, they are also deformed transversely by the spanwise velocities present in the buffer layer. These are of the order of $w'^+ \approx 1$ (Kim *et al.* 1987), but only $w'^+ \approx 0.5$ is at wavelengths long and wide enough to influence the meandering. The same order of magnitude is obtained by estimating the spanwise drift of the vortices under the induction of their reflected images across the wall. The resulting peak-to-peak meandering amplitude would be $\lambda_z = 2\sqrt{2}w't$, where t is the lifetime of the streaks. The latter can be expressed as $t = \lambda_x/S\Delta_z$ from the argument leading to (4.6), and we finally obtain

$$\lambda_z^+ \approx \sqrt{2}w'^+ \left(4\pi^2\lambda_x^2/\gamma S^2\right)^{+1/3} \approx 0.7\lambda_x^{+2/3}. \tag{4.7}$$
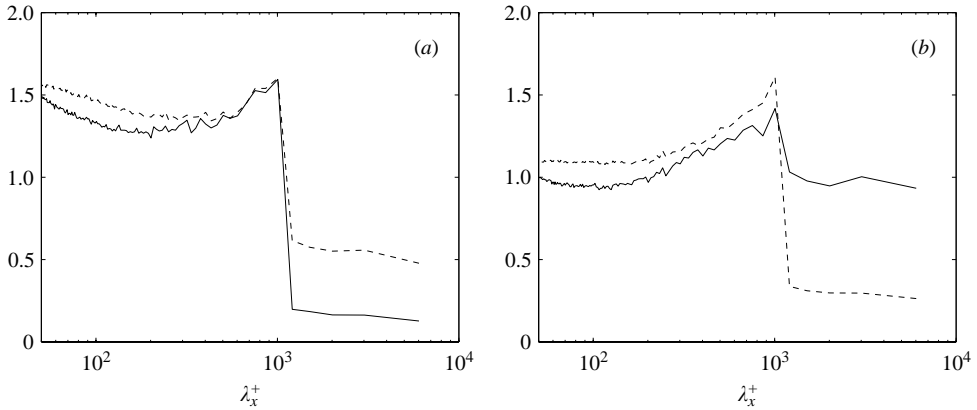
FIGURE 10. Ratio between the one-dimensional spectra of two simulations, one of which is the reference one C3, and the other one in which all the wavelengths larger that $\lambda_x^+ = 1200$ have been filtered at all heights in one of the two evolution equations. Averaged over $y^+ = 2$–35. ——, E_{vv}; – – – –, $E_{\omega_y \omega_y}$. (a) Filter in ϕ. (b) Filter in ω_y.

This estimate is included in figure 8(a) and represents well the behaviour of the bounding boxes for the streaks.

4.3. *Active or passive streaks*

In a linearized approximation, the equations for ω_y and ϕ are the Squire and Orr–Sommerfeld equations of stability theory (Schmid & Henningson 2001), and their relation is hierarchical. The equation for ω_y is in that case forced by v, which is in turn determined by an autonomous eigenvalue problem for ϕ. Such a one-way coupling is unlikely in turbulent flows, since both equations are known to be involved in a fully nonlinear regeneration cycle at the scales of the turbulent energy production, but it is not clear whether the very long ω_y streaks considered here are also active in the sense of participating in a large-scale version of such a cycle, or whether they are passive by-products of v.

That question can be addressed by numerical experiments in which both evolution equations are filtered independently. In figure 10 we show the results of two simulations in which, in addition to the numerical mask for the outer flow, one or the other equation has been masked at all heights for all the wavelengths longer than $\lambda_x^+ \approx 1200$, about twice as long as the turbulence-producing structures. It was shown by Jiménez & Pinelli (1999) that disrupting the cycle at wavelengths of the order of the production peak laminarizes the flow but that, as long as the peak is preserved, turbulence survives. That is the case in the present experiments, even though the masked wavelengths are responsible for about half of the energy production.

Figure 10 displays the ratio of the one-dimensional spectra of the masked case to the unmasked one. The results of the experiment in which only the ϕ-equation is masked at long wavelengths are shown in figure 10(a). Those of the dual one, in which only the ω_y equation is masked, are given in figure 10(b). While masking ϕ has a strong effect on ω_y, the converse is not true, and the evolution of ϕ is relatively independent of the masking of ω_y. This supports the one-way coupling mentioned above for the linear case, although only for the long structures, and shows that the generation of the streaks by the vertical velocity is still active at those wavelengths. The sharpness of the transition between masked and unmasked wavenumbers in the

spectra for ω_y in figure 10(a) suggests that the effect of the normal velocity on the streaks is local in the streamwise wavenumber, and therefore essentially linear.

To the left of the mask the ratio of the two spectra is roughly constant, implying that the dynamics of those scales is not strongly modified by the weakening of the large structures. There is however in all cases a slight rise just to the left of the discontinuity which suggests an energy cascade from small to large scales, whose blocking causes a bottleneck effect similar to the one observed near the dissipative range of isotropic turbulence (Falkovich 1994). Note that, because the Reynolds stresses are damped at the long wavelengths in both cases, the total shear stress decreases by about a factor of 2/3, and the normalized value of the spectra in the unmasked region increases accordingly.

4.4. *Outer–inner interactions*

A last question that has to be addressed is what the present observations imply about the effect of the outer flow on the near-wall layer. We started this paper by noting that the length of the velocity spectra scales as a multiple of the flow thickness in full-depth turbulent flows, and is therefore almost certainly controlled by the size of the outer structures. This is consistent with the observation by del Álamo & Jiménez (2003) that the very large structures are correlated across the whole channel, and that there is, in that sense, no difference between inner and outer flow at those wavelengths. We have also seen that the longest and widest structures are correlated across the full domain in the autonomous simulations, including the potential region. As in the previous case this suggests that those structures cannot be studied independently from the potential dynamics of the core. From that point of view the autonomous simulations are not 'pure' representations of the near-wall layer of full flows, but a different turbulent flow with a different upper boundary condition.

Nevertheless, the observation that the maximum lengths of the structures scale in outer units near the wall of the full simulations, while they are essentially infinite in autonomous ones, suggests that the rotational core fluctuations are more effective in disturbing the wall structures than the irrotational ones of the autonomous model. This goes beyond the existence of a definite outer length scale in the former case. Numerical experiments in which an outer scale was introduced in the autonomous simulations by substituting the infinitely deep potential domain by a no-slip condition at a given distance from the wall, failed to shorten the spectra. The most likely explanation is that rotational fluctuations have their own dynamics, while potential ones are governed by an instantaneous Laplace's equation, and are enslaved to the near-wall flow. In this sense the effect of the outer region in the full-depth flows can be described as shortening the 'infinitely' long autonomous wall structures to lengths of the order of the flow thickness, instead of as promoting their formation.

We can also say something about the scaling of the velocity fluctuations within the buffer layer. The classical theory is that all the turbulence intensities scale with u_τ in that region, but we saw in the introduction that there is experimental evidence for a weak dependence with Re_τ. DeGraaff & Eaton (2000) showed that, while the maximum of v'^{+2} reaches a constant asymptote at large Reynolds numbers, that of u'^{+2} is proportional to the free-stream velocity U_c, which at high Reynolds numbers increases as $\log(Re_\tau)$. Assume that the scale for the near-wall velocity fluctuations is some u_0, not necessarily equal to u_τ. We have seen in figure 7(a) that the spectral density for v is flat for long wavelengths. Its one-dimensional spectrum can be obtained by integrating $k_z E_{vv}^{2D}$ over the triangular wavelength region in that figure,

giving

$$E_{vv}^{1D}(k_x) \sim u_0^2 \int^\infty \lambda_z^{-1} \, \mathrm{d}\log(\lambda_z) \sim u_0^2, \tag{4.8}$$

with at most logarithmic corrections. On the other hand, the long spectra of u in figure 3(a) suggest a flat premultiplied spectrum, or

$$E_{uu}^{1D}(k_x) \sim u_0^2 k_x^{-1}. \tag{4.9}$$

We also saw in our discussion of the cospectrum that the cross-correlation coefficient of u and v becomes unity for long wavelengths, which implies that the long-wave cospectrum has the form

$$-E_{uv}^{1D}(k_x) \approx \left(E_{uu}^{1D} E_{vv}^{1D}\right)^{1/2} \sim u_0^2 k_x^{-1/2}. \tag{4.10}$$

The wall stress is obtained by integrating (4.10), which is integrable at $k_x = 0$, giving

$$u_\tau^2 = -\int_0 E_{uv}^{1D} \, \mathrm{d}k_x \sim u_0^2 \int_0 k_x^{-1/2} \, \mathrm{d}k_x \sim u_0^2, \tag{4.11}$$

and $u_0 = u_\tau$. A similar integration of (4.8) confirms that $v' \sim u_\tau$, but the u-spectrum in (4.9) is not integrable, and we have to consider the integration limits which, from figure 1, are $\lambda_x^+ \approx (500, 10Re_\tau)$. The result is

$$u'^2 = \int E_{uu}^{1D} \, \mathrm{d}k_x \sim u_\tau^2 \log(Re_\tau), \tag{4.12}$$

which agrees with DeGraaff & Eaton (2000). This result only takes into account the lengthening of the structures with the Reynolds number, but not the direct effect of the outer flow in the form of wide structures reaching the wall, whose kinetic energy would have to be included in (4.12). This contribution is negligible at the moderate Reynolds numbers of the comparison simulation F0, but del Álamo *et al.* (2004a) showed that the intensity of the outer structures scales with U_c instead of with u_τ. Its contribution to (4.12) would then be proportional to $\log^2(Re_\tau)$, and could become dominant at sufficiently high Reynolds numbers, as proposed by Hunt & Morrison (2000). Del Álamo *et al.* (2004a), however, argued that this is not necessarily the case, and a sharper version of their argument is given next. The large structures have velocities and length scales U_c and h. They are therefore essentially inviscid except near the wall, where they form viscous Stokes layers which grow for times of the order of h/U_c, and whose thicknesses are therefore $\delta_v \sim (\nu h/U_c)^{1/2}$. Assuming that the velocity gradient within those layers is more or less uniform, the fluctuations at a given y are of the order

$$u_{out}^+ = U_c^+ y/\delta_v = (U_c^+)^{3/2} y^+/Re_\tau^{1/2}, \tag{4.13}$$

whose contribution to u'^2 at a fixed y^+ is of order $u_{out}^2 \sim u_\tau^2 Re_\tau^{-1} \log^3(Re_\tau)$, and remains negligible with respect to (4.12) for all Re_τ.

5. Conclusions

We have seen that the small-scale structures of the near-wall region organize themselves into much larger scales, especially visible in the spectrum of the streamwise velocity component and in the Reynolds-stress cospectrum. It was shown by del Álamo & Jiménez (2003) that, in full-channel simulations, this part of the flow can

be separated into two components: narrow structures that scale in wall units and which are only correlated across the buffer layer, and wider ones with spanwise and streamwise wavelengths of the order of the flow thickness that are correlated across the full channel height.

We have shown that the narrow structures with $\lambda_x \gg \lambda_z$ are autonomous at all scales, in the sense of surviving with little change even in simulations in which the outer flow is numerically removed, but that the wider component is absent from the autonomous simulations, and is clearly connected with the effect of the outer flow.

This makes the autonomous simulations in this paper a good laboratory in which to study the long narrow structures in isolation, without interference from the outer dynamics.

We have shown that most of the v-spectrum can be understood in terms of a more or less random superposition of short wall-normal velocity structures, with dimensions of the order of $\lambda_x^+ \times \lambda_z^+ = 300 \times 50$ and advection velocities $c^+ \approx 10$. We have associated them with the quasi-streamwise vortices often described in the literature. Their intensity peaks within the buffer layer, and agrees well with the full simulations when the latter are filtered within the same range of spanwise wavenumbers. Wider and longer v-structures extend beyond the buffer layer, and are truncated by the numerical mask in the autonomous simulations.

The streamwise velocity is organized into streaks with lateral spacing $\lambda_z^+ \approx 100$, which are infinitely long within the extent of our simulations. We have shown that they are wakes left by the buffer-layer vortices as they move through the mean velocity shear, and that this model describes well the relation between their lengths and their widths. The analysis of the relative positions of the v- and u-structures suggests that the wakes of individual vortices do not extend beyond about $\lambda_x^+ \approx 1000$, and that the much longer streaks observed in the long-wavelength end of the u-spectrum are formed by coalescence of several shorter ones. Each of them is associated with several v-structures.

By identifying the dynamics of the vortices and of the streaks with the evolution of $\nabla^2 v$ and ω_y, we have studied their interactions by manipulating both equations independently. The vortices and the streaks are known to be involved in a nonlinear mutual regeneration cycle at scales of the order of the length of the vortices, but we have shown that the cycle is broken for wavelengths longer than 1000 wall units, beyond which the streaks do not feed back into vortex formation. The dynamics of these long structures are essentially two-dimensional in the (z, y) cross-plane, and they do not cascade energy into shorter wavelengths. They can, however, still extract energy from the mean flow, and almost half of the total Reynolds stresses resides in them.

Note that this two-dimensional behaviour explains why channel simulations with very short and narrow boxes have approximately correct velocity statistics, even if, for example, the numerical boxes of the minimal channels of Jiménez & Moin (1991), $L_x^+ \times L_z^+ = 400 \times 100$, are smaller than most of the u-spectrum in figure 3. The long structures are represented in those simulations by the infinitely long modes with $k_x = 0$.

We have finally argued that the effect of the outer flow on the near-wall streaks is to limit their lengths to some multiple of the boundary layer thickness, by shortening the otherwise infinitely long structures to be the same order as the outer-flow rotational eddies. We have shown that this implies a k_x^{-1} streamwise energy spectrum and a near-wall peak of u'^{+2} which increases with the logarithm of the Reynolds number. We have shown that this is true even in the presence of outer structures which reach

the wall, because viscosity should damp them below $\delta^+ \sim Re_\tau^{1/2}$, but that the scaling of the energy could be different above that height.

REFERENCES

DEL ÁLAMO, J. C. & JIMÉNEZ, J. 2003 Spectra of the very large anisotropic scales in turbulent channels. *Phys. Fluids.* **15**, L41–L44.

DEL ÁLAMO, J. C., JIMÉNEZ, J., ZANDONADE, P. & MOSER, R. D. 2004a Scaling of the energy spectra of turbulent channels. *J. Fluid Mech.* **500**, 135–144.

DEL ÁLAMO, J. C., JIMÉNEZ, J., ZANDONADE, P. & MOSER, R. D. 2004b The organization of the logarithmic and outer regions of turbulent channels. In preparation.

BULLOCK, K. J., COOPER, R. E. & ABERNATHY, F. H. 1978 Structural similarity in radial correlations and spectra of longitudinal velocity fluctuations in pipe flow. *J. Fluid Mech.* **88**, 585–608.

CORRAL, R. & JIMÉNEZ, J. 1995 Fourier/Chebyshev methods for the incompressible Navier Stokes equations in infinite domains. *J. Comput. Phys.* **121**, 261–270.

DEGRAAFF, D. B. & EATON, J. K. 2000 Reynolds number scaling of the flat-plate turbulent boundary layer. *J. Fluid Mech.* **422**, 319–346.

FALKOVICH, G. 1994 Bottleneck phenomenon in developed turbulence. *Phys. Fluids* **6**, 1411–1414.

HITES, M. M. 1997 Scaling of high-Reynolds-number turbulent boundary layers in the National Diagnostic Facility. PhD Thesis. Illinois Inst. of Technology.

HUNT, J. C. R. & MORRISON, J. F. 2000 Eddy structures in turbulent boundary layers. *Eur. J. Mech. B – Fluids* **19**, 673–694.

JIMÉNEZ, J. 1998 The largest scales of turbulent wall flows. In *CTR Ann. Res. Briefs, Stanford University*, pp. 137–154.

JIMÉNEZ, J., FLORES, O. & GARCÍA-VILLALBA, M. 2001 The large-scale organization of autonomous turbulent wall regions. In *CTR Ann. Res. Briefs, Stanford University*, pp. 317–328.

JIMÉNEZ, J. & MOIN, P. 1991 The minimal flow unit in near wall turbulence. *J. Fluid Mech.* **225**, 221–240.

JIMÉNEZ, J. & PINELLI, A. 1999 The autonomous cycle of near wall turbulence. *J. Fluid Mech.* **389**, 335–359.

JIMÉNEZ, J. & SIMENS, M. P. 2001 Low-dimensional dynamics in a turbulent wall. *J. Fluid Mech.*, **435**, 81–91.

KAWAHARA, G. & KIDA, S. 2001 Periodic motion embedded in plane Couette turbulence: regeneration cycle and burst. *J. Fluid Mech.* **449**, 291–300.

KIM, J. & HUSSAIN, F. 1993 Propagation velocity of perturbations in channel flow. *Phys. Fluids* A **5**, 695–706.

KIM, J., MOIN, P. & MOSER, R. 1987 Turbulence statistics in fully developed channel flow at low Reynolds number. *J. Fluid Mech.* **177**, 133–166.

KIM, K. C. & ADRIAN, R. J. 1999 Very large-scale motion in the outer layer. *Phys. Fluids* **11**, 417–422.

KROGSTAD, P.-A., KASPERSEN, J. H. & RIMESTAD, S. 1998 Convection velocities in turbulent boundary layers. *Phys. Fluids.* **10**, 949–957.

LAUFER, J., & NARAYANAN, M. A. B. 1971 Mean period of the turbulent production mechanism in a boundary layer. *Phys. Fluids* **14**, 182–83.

METZGER, M. M. & KLEWICKI, J. C. 2001 A comparative study of near-wall turbulence in high and low Reynolds numbers boundary layer. *Phys. Fluids* **13**, 692–701.

METZGER, M. M., KLEWICKI, J. C., BRADSHAW, K. L. & SADR, R. 2001 Scaling of near-wall axial turbulent stress in zero pressure gradient boundary layer. *Phys. Fluids* **13**, 1819–1821.

MORRISON, J. F., JIANG, W., MCKEON, B. J. & SMITS, A. J. 2002*a* Reynolds number dependence of streamwise velocity fluctuations in turbulent pipe flow. *AIAA Paper* 2002-0574.

MORRISON, J. F., JIANG, W., MCKEON, B. J. & SMITS, A. J. 2002*b* Reynolds number dependence of streamwise velocity spectra in turbulent pipe flow. *Phys. Rev. Lett*. **88**, 214501/1–4.

NAGATA, M. 1990 Three-dimensional finite-amplitude solutions in plane Couette flow: bifurcation from infinity. *J. Fluid Mech.* **217**, 519–527.

ORLANDI, P. & JIMÉNEZ, J. 1994 On the generation of turbulent wall friction. *Phys. Fluids* **6**, 634–641

ÖSTERLUND, J. M. 1999 Experimental studies of zero pressure-gradient turbulent boundary layer flow. PhD Thesis, Royal Inst. Mech. Stockholm.

ÖSTERLUND, J. M., JOHANSSON, A. V., NAGIB, H. M. & HITES, M. H. 2000 Spectral characteristics of the overlap region in turbulent boundary layers. Extended abstract to *Intl Congr. Theor. Appl. Math. 2000, Chicago*.

PERRY, A. E., HENBEST, S. & CHONG, M. S. 1986 A theoretical and experimental study of wall turbulence. *J. Fluid Mech* **165**, 163–199.

ROBINSON, S. K. 1991 Coherent motions in the turbulent boundary layer. *Annu. Rev. Fluid Mech.* **23**, 601–639.

SCHMID, P. J. & HENNINGSON, D. S. 2001 *Stability and Transition in Shear Flows*. Springer.

SHAH, D. A. & ANTONIA, R. A. 1989 Scaling of the bursting period in turbulent boundary layer and duct flow. *Phys. Fluids* A **1**, 318–25.

TOWNSEND, A. A. 1976 *The Structure of Turbulent Shear Flow*, 2nd. ed, p. 135. Cambridge University Press.

WALEFFE, F. 1998 Three-dimensional coherent states in plane shear flows. *Phys. Rev. Lett*. **81**, 4140–4143.

WALEFFE, F. 2001 Exact coherent structures in channel flow. *J. Fluid Mech.* **435**, 93–102.

WILLS, J. A. B. 1964 On convection velocities in turbulent shear flows. *J. Fluid Mech.* **20**, 419–432.